**Final Project Report, NSF Award 1461574**

# Collaborative Research: Low-cost imaging and analysis of the August 24, 2014 M6.1 South Napa California earthquake surface rupture (RAPID)

Edwin Nissen

Department of Geophysics, Colorado School of Mines, Golden CO 80401

10/1/2014–1/31/2016

## Summary

The goals of this project were to characterize surface offsets and off-fault deformation generated by the 24 August 2014 moment magnitude ($M_w$) 6.0 South Napa (California) earthquake using state-of-the-art topographic mapping and differencing techniques. This was the first ground-rupturing earthquake within the United States since the advent of 'structure-from-motion' photogrammetry in the early 2010s, and also the first within the US, and only the fifth globally, with both pre- and post-event light detection and ranging (lidar) coverage. At Colorado School of Mines, our contribution to the project was to apply and adapt nascent topographic differencing techniques to the repeat lidar point clouds in order to map the combined coseismic/early postseismic surface deformation field. In this respect, the South Napa earthquake posed several clear challenges to us. (1) The expected surface displacements (less than ∼0.25 m in an external reference frame) are small with respect to those generated by previous earthquakes mapped using differential lidar, which were much larger ($M_w$ 6.9–7.2) and generated surface displacements exceeding 1 m. (2) Furthermore, horizontal displacements in the South Napa event are expected to far exceed vertical displacements, yet our previous experience shows that lidar differencing is significantly better at measuring vertical than horizontal deformation. (3) The location of the rupture within an region of mixed intensive agriculture/suburban development is likely to have resulted in changes to the two lidar point clouds — collected in February 2003 and September 2014 and thus >11 years apart and in opposing seasons — that are unrelated to tectonic deformation. (4) Differences in the processing and classification of the two lidar points clouds further complicates their direct comparison. Ultimately, only the $y$-axis (N–S) component of the 3-D displacement field shows a coherent signal aligned with the known surface rupture, consistent with up to ∼0.4 m of right-lateral displacement. However, the ICP displacements also exhibit ∼0.5 m-amplitude noise over short wavelengths, obscuring any useful constraints on distributed deformation or damage zone properties. Though disappointing, this result does highlight the importance of collecting repeat lidar datasets at shorter intervals along active faults within areas undergoing rapid anthropogenic change, and also further motivates standardizations and refinements of point cloud classification and differencing techniques.

# 1 Introduction

The $M_w$ 6.0 South Napa earthquake occurred at 03:20 a.m. PDT on 24 August 2014 and was the largest event to strike the San Francisco Bay area in a quarter of a century (*Brocher et al.*, 2015). The earthquake generated almost purely dextral motion along several strands of the West Napa fault zone, part of a network of NNW-trending strike-slip faults that accomodate Pacific–North America plate motions north of San Francisco Bay. Prior to the earthquake, the West Napa fault zone had not experienced a major earthquake during instrumental or historical times. Though recognized as being active (*Wesling and Hanson*, 2008) it was otherwise only poorly characterized, with no firm constraints from quantitative dating on either its slip rate or paleoseismic record. The 2014 earthquake therefore provided rich new data on the kinematics of the West Napa fault zone, and its surface rupture also incorporated fault strands that had not previously been recognized at all.

The main rupture trace follows the Brown's Valley strand of the West Napa fault zone over a distance of ∼12–14 km, from Green Island in the Napa river delta in the South to the western suburbs of Napa city in the North (*Brocher et al.*, 2015; *Morelan et al.*, 2015). The earthquake generated up to 46 cm of right-lateral surface slip along the northern half of the fault, whereas offsets along southern half were initially limited to ∼20 cm from combined coseismic and immediate postseismic slip. However, surface offsets in the South grew rapidly over the following several weeks due to afterslip, eventually nearly matching those from the North (*DeLong et al.*, 2015; *Lienkaemper et al.*, 2016; *Floyd et al.*, 2016). Dip slip along the main rupture trace was at most a few centimeters, although early postseismic deformation measured at one location in the South revealed a ∼15 cm vertical (up to the West) 'warping' accommodated within a few 10s of meters of the main surface break (*DeLong et al.*, 2015). Slip on fault strands adjacent to the Brown's Valley fault was limited to a few centimeters.

Seismological and space geodetic data indicate almost pure dextral slip on a steep (∼80–85°), W-dipping fault plane (e.g. *Barnhart et al.*, 2015; *Brocher et al.*, 2015; *Dreger et al.*, 2015; *Feng et al.*, 2015; *Melgar et al.*, 2015; *Wei et al.*, 2015; *Floyd et al.*, 2016). Many of the geodetic inversions place peak slip of ∼1 m at depths of ∼1–4 km, which implies a significant shallow slip deficit given the maximum surface offsets of around half this value. The seismology also reveals that the rupture initiated at a depth of 10-11 km in an area of low eventual slip, before propagating unilaterally upwards and towards the NNW (*Wei et al.*, 2015; *Ji et al.*, 2015). Subsequent aftershocks also concentrate below the main rupture plane in an area of low mainshock slip (*Wei et al.*, 2015). These patterns of coseismic, post-seismic and aftershock deformation — together with the availability of dense geodetic and seismological observations and the success in computing near real-time fault plane solutions from these data (*Grapenthin et al.*, 2014) — helped generate widespread scientific interest in the South Napa earthquake in spite of its moderate magnitude.

To enhance the governmental and scientific response to the earthquake, airborne lidar data were collected along a ∼3 km wide, ∼18 km-long swath centered along the main surface rupture (Figure 1). The survey was undertaken on 9 September 2014 by Towill, Inc., using an Optech Orion M300 scanner and a combination of temporary GPS deployments and Plate Boundary Observatory stations for ground control. The point cloud was later reprocessed and reclassified by the USGS, and it averages ∼22.5 points/m$^2$. On 1 February 2003, the entire Napa watershed was mapped with lidar by the National Center for Airborne Laser Mapping (Figure 1). The 2003 lidar survey averages ∼1.5 points/m$^2$ (last returns only) and fully encloses the extents of the 2014 dataset.

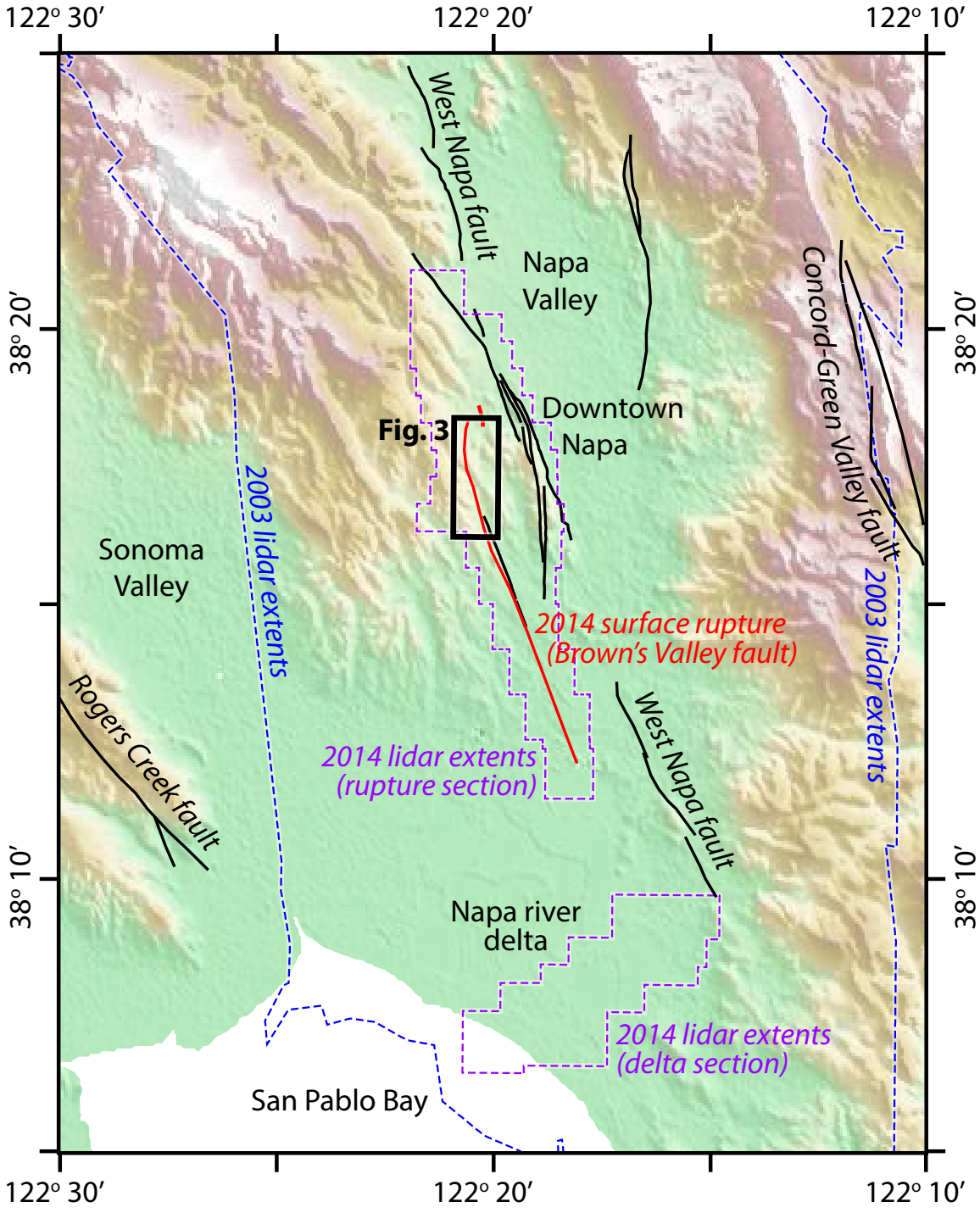


Figure 1: 2003 and 2014 lidar coverage (blue and purple polygons, respectively) and active faulting in the Napa Valley region. The surface trace of the 2014 South Napa earthquake is marked in red (*Morelan et al.*, 2015). Other active faults from the USGS Quaternary Fault and Fold Database are shown in black (*Haller et al.*, 2004).

However, only the last return data were initially classified; the full unfiltered (first and last return) data were later released in response to the South Napa earthquake, but these were left unclassified.

The were two main aims of this NSF RAPID project. Firstly, we wanted to characterize surface offsets using state-of-the-art photogrammetric mapping techniques ('structure-from-motion'). This work was led by PI Michael Oskin at University of California Davis and early results were published in *Morelan et al.* (2015); the role of co-PI Edwin Nissen and graduate student Kendra Johnson at Colorado School of Mines was merely advisory, having led recent development of structure-from-motion protocols with rapid-response mapping in mind (*Johnson et al.*, 2014). Secondly, we hoped to map off-fault deformation by differencing the pre- and post-earthquake airborne lidar topography. The South Napa earthquake is the only fifth ground-rupturing earthquake (and the first within the United States) with at least partial pre- and post-event airborne lidar coverage, following the 2008 Iwate-Miyagi, Japan ($M_w$ 6.9), 2010 El Mayor-Cucapah, Mexico ($M_w$ 7.2), 2010 Darfield, New Zealand ($M_w$ 7.1) and 2011 Fukushima-Hamadori, Japan ($M_w$ 7.1) earthquakes (*Mukoyama*, 2012; *Oskin et al.*, 2012; *Duffy et al.*, 2013; *Glennie et al.*, 2014; *Nissen et al.*, 2014). Jointly, the PI and co-PIs on this award have worked on most of these earlier events; our role at Colorado School of Mines was to apply and adapt our recently-developed topographic differencing techniques to the South Napa event (*Nissen et al.*, 2012, 2014).

## 2 Methods

We mapped surface deformation within the South Napa rupture zone by differencing pre- and post-event lidar point clouds using an adaptation of the Iterative Closest Point (ICP) algorithm (*Chen and Medioni*, 1991; *Besl and McKay*, 1992). ICP registers (aligns) 'model' and 'target' point cloud representations of the same surface through iterative application of a rigid-body transformation, comprising a three-component translation and a three-component rotation. Each single iteration minimizes the average distance between each point in the model surface and either its closest neighbour in the target surface ('point-to-point' ICP), or planar representations of the target points ('point-to-plane' ICP). Once further iterations cease to reduce the average closest point pair distances, the procedure halts and the cumulative rigid-body transformation is calculated. The translation components represent the displacements that most closely align the model point cloud with the target cloud.

In our own adaptation for mapping surface deformation from lidar data (*Nissen et al.*, 2012, 2014), we first split each point cloud into square cells with prescribed dimensions before applying ICP to each equivalent (pre-event/model and post-event/target) pair of cells (Figure 2). Because ICP alignments are hampered by edge effects, an additional 'fringe' of points is included in each post-event cell such that it fully encloses the equivalent pre-event points, including accounting for their likely coseismic displacement. Past experience indicates that point-to-plane ICP variants (*Chen and Medioni*, 1991) cope best in registering irregular point clouds of highly disparate density. Additionally, we implemented a 'sparse ICP' approach (*Bouaziz et al.*, 2013), in which points are iteratively reweighted in order to reduce the influence of outliers.

The choice of cell size represents a trade-off between two competing factors. On the one hand, cells must be large enough that they contain sufficient relief for ICP to produce robust displacements, since roughly planar surfaces containing minimal relief might be aligned equally well using a variety of transformations. On the other hand, cells must be small enough that any internal deformation,

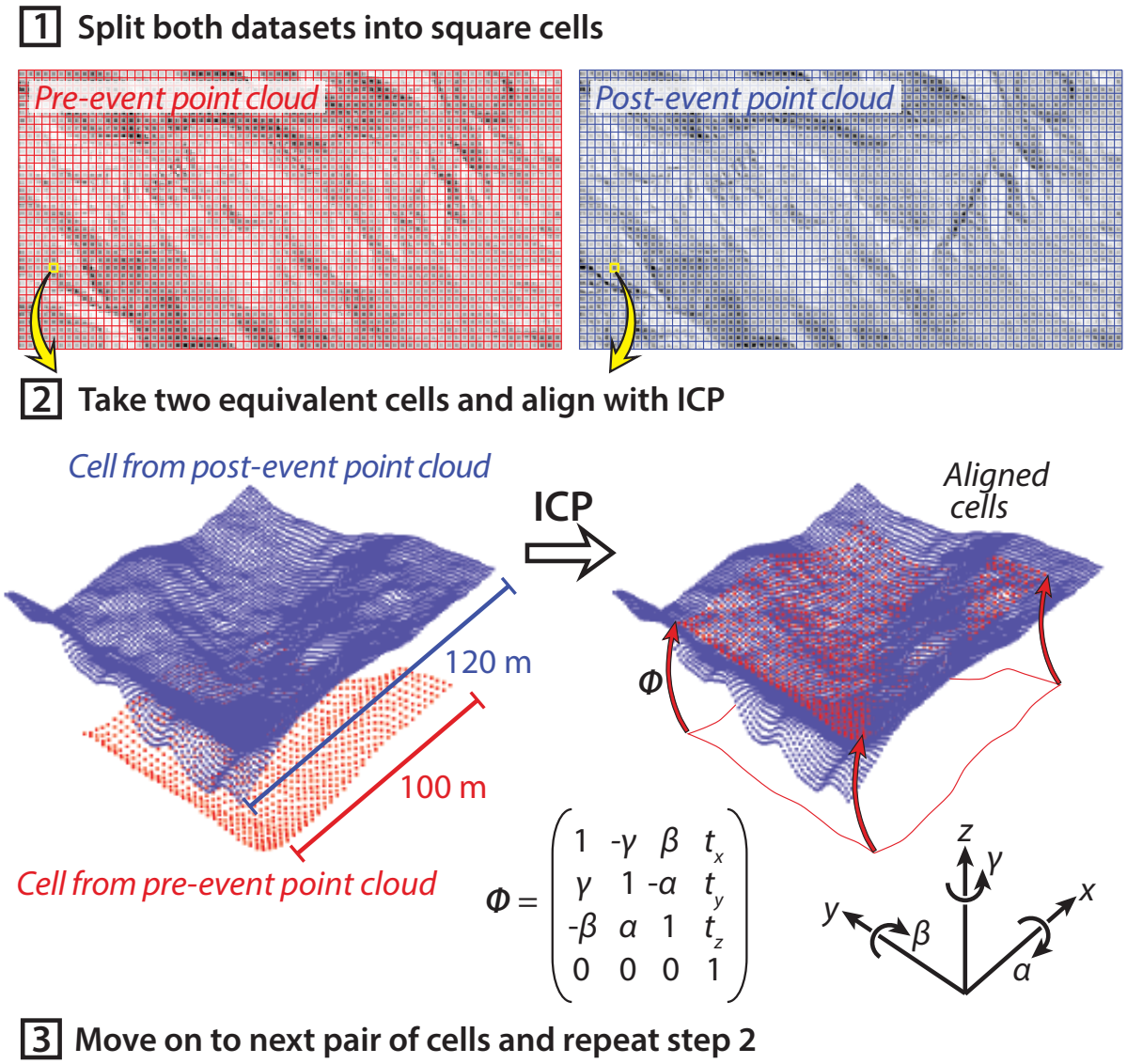


Figure 2: Outline of our method for aligning pre- and post-event point cloud cells, based on an adaptation of the Iterative Closest Point (ICP) algorithm (*Nissen et al.*, 2012). In step 2, the rigid body transformation $\Phi$ that minimizes closest point distances between the pre- and post-event cells comprises translations $t_x$, $t_y$ and $t_z$ in the $x$, $y$ and $z$ directions, and rotations $\alpha$, $\beta$ and $\gamma$ about the $x$, $y$ and $z$ axes. This figure is modified from *Nissen et al.* (2014).

such as that arising from steep coseismic displacement gradients close to an earthquake surface rupture, has insignificant bearing on the rigid body transformation employed in the ICP procedure. Here, we used cell sizes of 50 × 50 m — dimensions that have proven to work well in past real earthquake examples (*Nissen et al.*, 2014; *Glennie et al.*, 2014) — with an additional 10 m-wide 'fringe' added to the post-event cells. In addition, application of a 'sliding window' approach allows us to increase the spatial resolution of the final displacement field to 25 × 25 m.

The choice of which subset of points to include in the ICP procedure is equally important. On the one hand, lidar returns representing vegetation or built infastructure (e.g. leaves, branches, fences, overhead power lines, vehicles, and buildings) may move, appear or disappear between the pre-event and post-event lidar aquisitions, thereby hampering alignment of the two point clouds. On the other hand, where such features are intransient, inclusion of these lidar returns may provide useful 'relief' that actually aids ICP registration. In the case of the South Napa earthquake, this choice is further complicated by the differing ways in which the 2003 and 2014 point clouds were filtered and classified (as described in the Introduction). At each of the prescribed cell sizes, we therefore ran ICP on two subsets of the lidar point clouds: (i) the complete, unfiltered 2003 and 2014 data, and (ii) classified ground returns only.

## 3 Results

Differencing of the classified ground return datasets gave more coherent displacements (with less scatter) than using the unfiltered point clouds, and so we focus on the former set of results. To illustrate, Figure 3 shows displacements from the northern ∼3.5 km of the main rupture strand — where field measurements and geodetic models indicate the highest surface slip occurred — up to the small (∼500 m) right-stepover in faulting in the Brown's Valley neighbourhood. Only the $y$-axis displacements show a signal clearly related to surface faulting, with positive values west of the fault trace indicating northwards motion relative to the approximately static eastern side of the fault (Figure 3, middle panel). $x$- and $z$-axis displacements show some coherent patterns and trends, but none that align consistently along the fault (Figure 3, left and right panels). However, the absence of E–W and vertical coseismic deformation is to be expected given the N–S fault strike and the almost pure right-lateral slip vector. All three components exhibit 'blotchy' artefacts, which we believe represent localized areas of landscape surface change, whether due to agriculture, urban development, or natural geomorphic processes.

Four swath profiles — from A–A' in the north to D–D' in the south — help to further characterize the ICP results (Figure 4). Horizontal $x$- and $y$-axis displacements exhibit scatter of ∼0.25–0.5 m, whereas vertical $z$-axis displacements are significantly cleaner, with scatter of only ∼0.1–0.25 m. This difference — which likely reflects (1) that the point clouds are more 'bunched' in the vertical dimension than in the horizontal dimensions and (2) that horizontal errors in raw lidar point positioning are worse than vertical errors — has been observed in ICP results for other earthquakes (*Glennie et al.*, 2014; *Nissen et al.*, 2014). Noise in the ICP results probably reflects a variety of factors. Western Napa Valley is a region of mixed intensive agriculture and suburban development, and so there may have been significant landscape changes between February 2003 and September 2014 that are unrelated to tectonic deformation. The >11 year timespan between lidar acquisitions is more than double those of past earthquakes with differential coverage (e.g. *Glennie et al.*, 2014; *Nissen et al.*, 2014), and furthermore seasonal changes may also be an influence. The fact that the two point clouds were processed and classified differently may also be important.

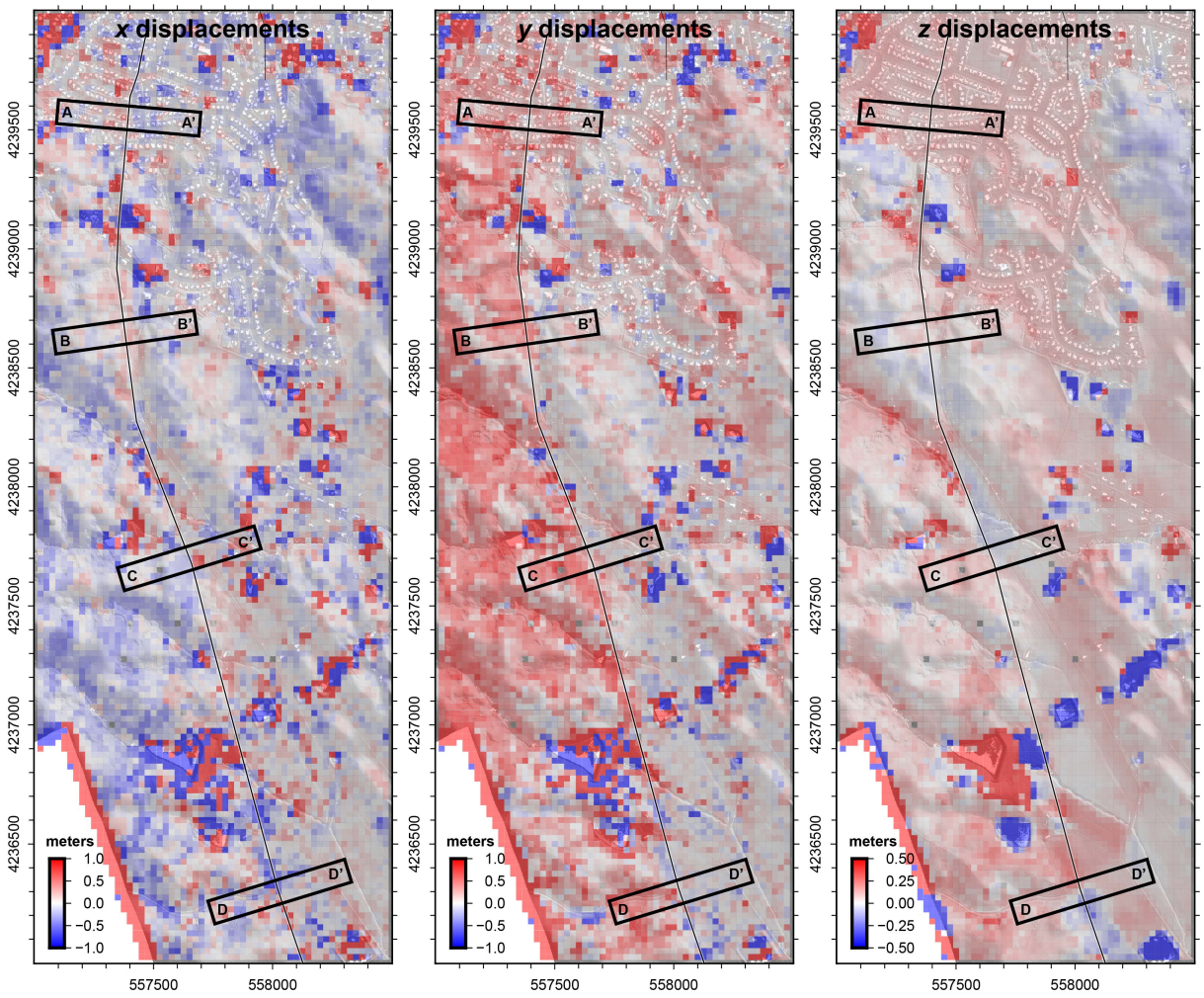


Figure 3: ICP results from differencing the 2003 and 2014 Napa valley airborne lidar topography using a cell size of 50 × 50 m, a window step of 25 m, and the classified ground returns. This figure targets the portion of the mapped surface rupture (thin black line) with the highest surface slip. Axes display UTM zone 10 coordinates in meters. (a) Displacements in the $x$ direction — positive is towards the East. (b) Translations in the $y$ direction — positive is towards the North. (c) Translations in the $z$ direction — positive is upwards. Thick black rectangles represent the swath profiles shown in Figure 4.

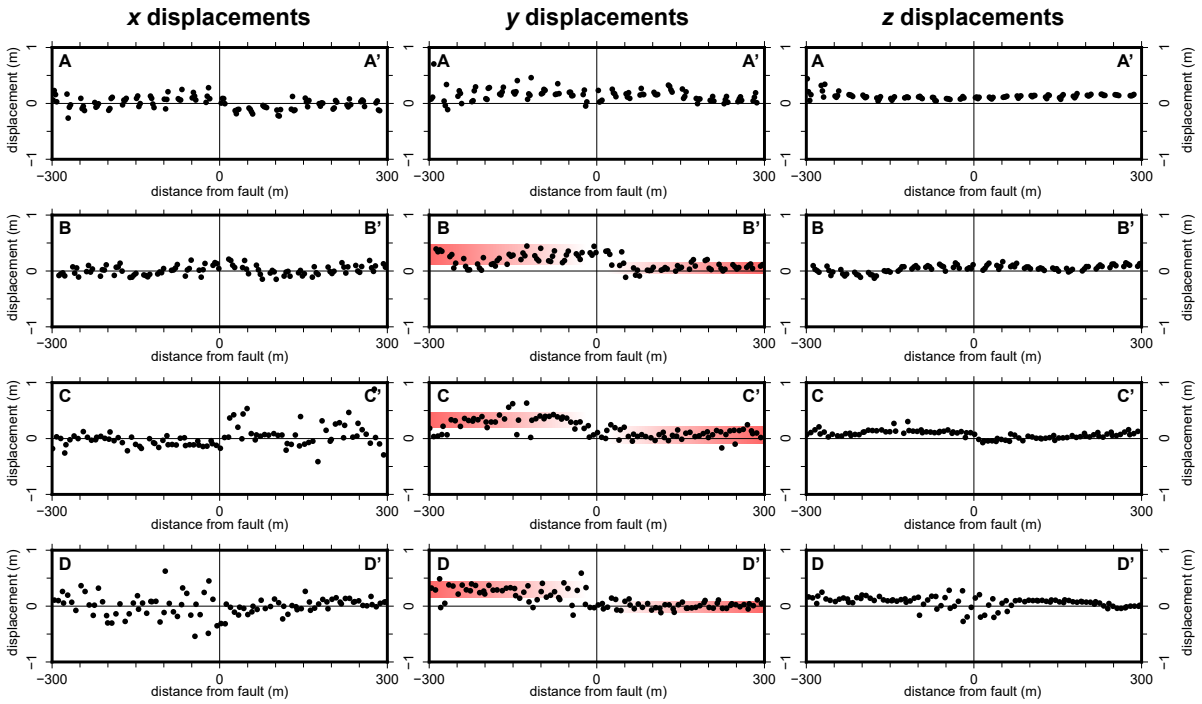


Figure 4: Swath profiles through the ICP displacement results shown in Figure 3. The left, middle and right columns show $x$-, $y$- and $z$-axis displacements respectively, and the rows show each of the four swaths indicated on Figure 3. Distances are shown relative to the surface rupture, with negative values lying to the west and positive values to the east.

Nevertheless, a ∼0.2–0.4 m discontinuity in $y$-axis displacements can be observed in profiles B–B', C–C' and D–D' (red shading, Figure 4), in approximate agreement with field and geodetic estimates of right-lateral surface slip in this area. However, the scatter prevents us from determining whether all of this slip is accommodated at the main rupture trace, or whether it is distributed over a wider damage zone, as has been inferred from other lidar deformation fields (*Nissen et al.*, 2014). The absence of a clear discontinuity in profile A–A' may be related to a reduction in localized slip within the stepover zone between the two fault strands.

Although the lidar-derived displacement field captures the known dextral fault offsets, the level of noise restricts what we can usefully do with these data. Right-lateral slip of ∼0.2–0.4 m on the northern Brown's Valley strand is clearly substantially smaller than the peak slip of ∼1 m inferred at depth (e.g. *Barnhart et al.*, 2015; *Wei et al.*, 2015; *Floyd et al.*, 2016), implying a shallow slip deficit — but this was already clear before our ICP analysis. The scatter in $y$-axis displacements precludes precise estimates of the 'surface slip ratio' (*Dolan and Haravitch*, 2014) or fault damage zone width.

# 4 Conclusions

3-D differencing of repeat airborne lidar point clouds spanning the 2014 South Napa earthquake captures the overall right-lateral sense of slip, and the approximate surface slip magnitude of up to ∼0.4 m. This confirms previous inferences of a significant shallow slip deficit between peak slip of ∼1 m at depths of ∼1–4 km and surface faulting. However, ∼0.25–0.5 m-level scatter in the displacement fields limits what more we can do with these data. This noise may reflect non-tectonic change between the two lidar surveys, which span >11 years and were collected in different seasons, or limitations arising from the disparate ways in which the two point clouds were classified.

# 5 Acknowledgments

This work was supported through National Science Foundation (Earthscope Program) RAPID award 1461574. Post-earthquake lidar data were funded by the California Department of Water Resources, the US Geological Survey, the California Geological Survey, and PEER-GEER. More information about the data collection and application can be found in U.S. Geological Survey Open-File Report 2014-1249. These lidar data were collected (9 September 2014), processed and delivered by Towill, Inc. under California Department of Water Resources (DWR) contract 4600008691. DWR and the other cost-share partners listed above shall not accept any liability for its accuracy, quality or suitability for use by any entity. Earlier Napa watershed lidar data were funded by the National Science Foundation and acquired on 1 February 2003 by the National Center for Airborne Laser Mapping (NCALM). Both lidar datasets are publically available through the NSF-supported OpenTopography portal. Sri Raghu Malireddi and Andrea Tagliasacchi are gratefully acknowledged for their help in implementing sparse ICP.

# References

Barnhart, W. D., J. R. Murray, S.-H. Yun, J. L. Svarc, S. V. Samsonov, E. J. Fielding, B. A. Brooks, and P. Milillo (2015), Geodetic constraints on the 2014 M 6.0 South Napa earthquake, *Seismol. Res. Lett.*, *86*, 335–343.

Besl, P. J., and N. D. McKay (1992), A Method for Registration of 3-D Shapes, *IEEE Trans. Pattern Anal. Mach. Intell.*, *14*(2), 239–256.

Bouaziz, S., A. Tagliasacchi, and M. Pauly (2013), Sparse iterative closest point, in *Computer graphics forum*, vol. 32, pp. 113–123.

Brocher, T. M., A. S. Baltay, J. L. Hardebeck, F. F. Pollitz, J. R. Murray, A. L. Llenos, D. P. Schwartz, J. L. Blair, D. J. Ponti, J. J. Lienkaemper, V. E. Langenheim, T. E. Dawson, K. W. Hudnut, D. R. Shelly, D. S. Dreger, J. Boatwright, B. T. Aagaard, D. J. Wald, R. A. Allen, W. D. Barnhart, K. L. Knudsen, B. A. Brooks, and K. M. Scharer (2015), The Mw 6.0 24 August 2014 South Napa Earthquake, *Seismol. Res. Lett.*, *86*, 309–326.

Chen, Y., and G. Medioni (1991), Object Modeling by Registration of Multiple Range Images, in *Proc. IEEE Int. Conf. on Robotics and Automation*, pp. 2724–2729.

DeLong, S. B., J. J. Lienkaemper, A. J. Pickering, and N. N. Avdievitch (2015), Rates and patterns of surface deformation from laser scanning following the South Napa earthquake, California, *Geosphere*, *11*, 1–80.

Dolan, J. F., and B. D. Haravitch (2014), How well do surface slip measurements track slip at depth in large strike-slip earthquakes? The importance of fault structural maturity in controlling on-fault slip versus off-fault surface deformation, *Earth Planet. Sci. Lett.*, *388*, 38–47.

Dreger, D. S., M.-H. Huang, A. Rodgers, T. Taira, and K. Wooddell (2015), Kinematic Finite-Source Model for the 24 August 2014 South Napa, California, Earthquake from Joint Inversion of Seismic, GPS, and InSAR Data, *Seismol. Res. Lett.*, *86*, 327–334.

Duffy, B., M. Quigley, D. J. A. Barrell, R. Van Dissen, T. Stahl, S. Leprince, C. McInnes, and E. Bilderback (2013), Fault kinematics and surface deformation across a releasing bend during the 2010 MW 7.1 Darfield, New Zealand, earthquake revealed by differential LiDAR and cadastral surveying, *Geol. Soc. Am. Bull.*, *125*, 420–431.

Feng, G., Z. Li, X. Shan, B. Xu, and Y. Du (2015), Source parameters of the 2014 Mw 6.1 South Napa earthquake estimated from the Sentinel 1A, COSMO-SkyMed and GPS data, *Tectonophys.*, *655*, 139–146.

Floyd, M. A., R. J. Walters, J. R. Elliott, G. J. Funning, J. L. Svarc, J. R. Murray, A. J. Hooper, Y. Larson, P. Marinkovic, R. Bürgmann, I. A. Johanson, and T. J. Wright (2016), Spatial variations in fault friction related to lithology from rupture and afterslip of the 2014 South Napa, California, earthquake, *Geophys. Res. Lett.*, *43*, 6808–6816.

Glennie, C. L., A. Hinojosa-Corona, E. Nissen, A. Kusari, M. E. Oskin, J. R. Arrowsmith, and A. Borsa (2014), Optimization of legacy lidar data sets for measuring near-field earthquake displacements, *Geophys. Res. Lett.*, *41*, 3494–3501.

Grapenthin, R., I. Johanson, and R. M. Allen (2014), The 2014 $M_w$ 6.0 Napa earthquake, California: Observations from real-time GPS-enhanced earthquake early warning, *Geophys. Res. Lett.*, *41*, 8269–8276.

Haller, K. M., M. N. Machette, R. L. Dart, and B. S. Rhea (2004), U.S. Quaternary Fault and Fold Database Released, *Eos Trans. AGU*, *85*, 218–218.

Ji, C., R. J. Archuleta, and C. Twardzik (2015), Rupture history of 2014 $M_w$ 6.0 South Napa earthquake inferred from near-fault strong motion data and its impact to the practice of ground strong motion prediction, *Geophys. Res. Lett.*, *42*, 2149–2156.

Johnson, K., E. Nissen, S. Saripalli, J. R. Arrowsmith, P. McGarey, K. Scharer, P. Williams, and K. Blisniuk (2014), Rapid mapping of ultrafine fault zone topography with structure from motion, *Geosphere*, *10*, 969–986.

Lienkaemper, J. J., S. B. DeLong, C. J. Domrose, and C. M. Rosa (2016), Afterslip behavior following the 2014 M 6.0 South Napa earthquake with implications for afterslip forecasting on other seismogenic faults, *Seismol. Res. Lett.*, *87*, 609–619.

Melgar, D., J. Geng, B. W. Crowell, J. S. Haase, Y. Bock, W. C. Hammond, and R. M. Allen (2015), Seismogeodesy of the 2014 $M_w$6.1 Napa earthquake, California: Rapid response and modeling of fast rupture on a dipping strike-slip fault, *J. Geophys. Res.*, *120*, 5013–5033.

Morelan, A. E., C. C. Trexler, and M. E. Oskin (2015), Surface-Rupture and Slip Observations on the Day of the 24 August 2014 South Napa Earthquake, *Seismol. Res. Lett.*, *86*, 1119–1127.

Mukoyama, S. (2012), Estimation of ground deformation caused by the earthquake (Mw 7.2) in Japan, 2008, from the geomorphic image analysis of high resolution LiDAR DEMs, *J. Mt. Sci.*, *8*, 239–245.

Nissen, E., A. K. Krishnan, J. R. Arrowsmith, and S. Saripalli (2012), Three-dimensional surface displacements and rotations from differencing pre- and post-earthquake LiDAR point clouds, *Geophys. Res. Lett.*, *39*, L16301.

Nissen, E., T. Maruyama, J. Ramon Arrowsmith, J. R. Elliott, A. K. Krishnan, M. E. Oskin, and S. Saripalli (2014), Coseismic fault zone deformation revealed with differential lidar: Examples from Japanese $M_w$ ∼7 intraplate earthquakes, *Earth Planet. Sci. Lett.*, *405*, 244–256.

Oskin, M. E., J. R. Arrowsmith, A. H. Corona, A. J. Elliott, J. M. Fletcher, E. J. Fielding, P. O. Gold, J. J. G. Garcia, K. W. Hudnut, J. Liu-Zeng, and O. J. Teran (2012), Near-Field Deformation from the El Mayor-Cucapah Earthquake Revealed by Differential LIDAR, *Science*, *335*, 702–705.

Wei, S., S. Barbot, R. Graves, J. J. Lienkaemper, T. Wang, K. Hudnut, Y. Fu, and D. Helmberger (2015), The 2014 Mw 6.1 South Napa earthquake: A unilateral rupture with shallow asperity and rapid afterslip, *Seismol. Res. Lett.*, *86*, 344–354.

Wesling, J., and K. Hanson (2008), Mapping of the West Napa fault zone for input into the northern California Quaternary fault database, *U.S. Geol. Surv. Open File Rep.*, 05HQAG0002.